Eur. Phys. J. A (2015) **51**: 7
DOI 10.1140/epja/i2015-15007-2

THE EUROPEAN PHYSICAL JOURNAL A

Regular Article – Theoretical Physics

Low-density homogeneous symmetric nuclear matter: Disclosing dinucleons in coexisting phases

Hugo F. Arellano[1,2,a] and Jean-Paul Delaroche[2]

[1] Department of Physics - FCFM, University of Chile, Av. Blanco Encalada 2008, Santiago, Chile
[2] CEA, DAM, DIF, F-91297 Arpajon, France

Received: 27 October 2014 / Revised: 12 January 2015
Published online: 28 January 2015 – © Società Italiana di Fisica / Springer-Verlag 2015
Communicated by K. Yabana

Abstract. The effect of *in-medium* dinucleon bound states on self-consistent single-particle fields in Brueckner, Bethe and Goldstone theory is investigated in symmetric nuclear matter at zero temperature. To this end, dinucleon bound state occurences in the ${}^1S_0$ and ${}^3SD_1$ channels are explicitly accounted for —within the continuous choice for the auxiliary fields— while imposing self-consistency in Brueckner-Hartree-Fock approximation calculations. Searches are carried out at Fermi momenta in the range $0 < k_F \leq 1.75\,\mathrm{fm}^{-1}$, using the Argonne v_{18} bare nucleon-nucleon potential without resorting to the effective-mass approximation. As a result, two distinct solutions meeting the self-consistency requirement are found with overlapping domains in the interval $0.130\,\mathrm{fm}^{-1} \leq k_F \leq 0.285\,\mathrm{fm}^{-1}$, corresponding to mass densities between $10^{11.4}$ and $10^{12.4}\,\mathrm{g\,cm}^{-3}$. Effective masses as high as three times the nucleon mass are found in the coexistence domain. The emergence of superfluidity in relationship with BCS pairing gap solutions is discussed.

1 Introduction

Dinucleon formation, pairing, clustering and condensation in nuclear media have been subjects of considerable research during the past few decades motivated by their role in heavy-ion collisions, collapsing stars, weakly bound nuclear systems and critical phenomena [1,2]. Even in their simplest conceptions, nuclear matter models may become exceedingly complex systems featuring strongly interacting Fermions over a broad range of conditions. Densities may vary from highly diluted systems, as in nuclear halos or envelopes of core-collapse supernovae, up to a few times the saturation density, as in the core of neutron stars. The isospin asymmetry can also vary from zero, as in symmetric nuclear matter, up to unity, as in pure neutron matter thought to prevail in the interior of neutron stars. Temperature can also be subject to wide variations from zero up to a few hundreds of MeV.

Among the various approaches to study interacting nucleons systems, the Brueckner-Hartree-Fock (BHF) approximation can be regarded as a reasonable starting point to investigate homogeneous infinite nuclear matter [3,4]. This approximation embodies important information upon which higher-order corrections can be incorporated [5]. However, it has long been recognized that bound states in BHF approximation signal the onset of superfluidity, phenomenon which needs to be investigated within a much broader framework [6]. Beyond this limitation, the question remains as to whether it is feasible to find self-consistent single-particle (sp) fields in infinite nuclear matter within BHF, accounting *simultaneously* for dinucleon bound states. In this work we address this issue by providing an explicit account for dinucleon bound states in the ${}^1S_0$ and ${}^3SD_1$ channels, expressed as isolated poles of the g matrix on the real axis below the continuum threshold, while seeking self-consistency in the sp potential. We have avoided the use of the effective mass approximation to represent the sp fields, aiming to rule out potential sources of ambiguities in our findings. Additionally, the sp momentum distribution follows a normal Fermi distribution, namely $n(k) = \Theta(k_F - k)$, with k_F the Fermi momentum. As a consequence we obtain two distinct solutions satisfying the self-consistency requirement in the range $0.13\,\mathrm{fm}^{-1} \lesssim k_F \lesssim 0.29\,\mathrm{fm}^{-1}$, *i.e.* matter densities between 1.5×10^{-4} and $2 \times 10^{-3}\,\mathrm{fm}^{-3}$, corresponding to mass densities of $10^{11.4}$ and $10^{12.4}\,\mathrm{g\,cm}^{-3}$, respectively. To investigate and resolve these features, special measures were needed to control singularities implied by bound states. Considering that at very low densities hole-hole ladder contributions become weak [7] due to the limited phase space they act upon, the results we obtain for nuclear densities below $10^{-3}\,\mathrm{fm}^{-3}$ based only on particle-particle (pp) contributions become reasonably justified within BHF alone, namely as long as effects associated with superfluidity are neglected. In any case, taking the present results as a baseline, the inclusion of

[a] e-mail: arellano@dfi.uchile.cl

hole-hole propagation beyond Brueckner ladder diagrams would need to be reassessed in another work.

Nuclear-matter properties have been extensively investigated in the framework of the Brueckner-Bethe-Goldstone (BBG) theory based on the hole-line expansion for the ground-state energy [8]. Here the Goldstone diagrams are grouped according to their number of hole lines, with each group summed up separately. The summation of the two-hole-line diagrams yields the usual BHF approximation, where the two-body scattering matrix in nuclear matter is calculated self-consistently with the sp energy spectrum. Although the sp potential is introduced only as an auxiliary quantity, its choice conditions the rate of convergence of the expansion for the binding energy. In ref. [9] it has been reported that the continuous choice [10–12] for the auxiliary potential provides better convergence over the so called *standard choice*, where the sp potential is set to zero above the Fermi energy. Hence, we shall use the continuous choice to investigate the role of dinucleon bound states during the search for self-consistent sp potentials.

This paper is organized as follows. In sect. 2 we outline the theoretical background upon which we address self-consistency in nuclear matter within the BHF approximation. In sect. 3 we succinctly describe special measures aimed to control numerical instabilities, particularly the treatment of dinucleon bound-state poles of the g matrix on the real axis. We also address the existence of multiple roots in the energy denominator of the propagator and describe procedures to handle sharp integrands. In sect. 4 we present and discuss solutions for the self-consistent sp fields, associated nuclear matter binding and effective masses. We also discuss the spatial properties of dinucleons as well as some immediate implications of the sp fields when applied in the context of pairing gap equations for superfluid states. In sect. 5 we present a summary of the work, draw its main conclusions and outlook.

2 Framework

In BBG theory for symmetric nuclear matter the g matrix depends on the density of the medium, characterized by the Fermi momentum k_F, and a starting energy ω. To the lowest order in the BHF approximation for nuclear matter in normal state, when only two-body correlations are taken into account, the g matrix satisfies

$$g(\omega) = v + v\,\frac{Q}{\omega + i\eta - \hat{h}_1 - \hat{h}_2}\,g(\omega)\,, \tag{1}$$

with v the bare interaction between nucleons, $\hat{h}_i$ the *sp* energy of nucleon i ($i = 1, 2$), and Q the Pauli blocking operator which in normal BHF takes the form

$$Q|\boldsymbol{p}\,\boldsymbol{k}\rangle = \Theta(p - k_F)\Theta(k - k_F)|\boldsymbol{p}\,\boldsymbol{k}\rangle\,.$$

The solution to eq. (1) enables the evaluation of the mass operator

$$M(k;E) = \sum_{|\boldsymbol{p}|\le k_F} \langle \frac{1}{2}(\boldsymbol{k}-\boldsymbol{p})|g_{\boldsymbol{K}}(E + e_p)|\frac{1}{2}(\boldsymbol{k}-\boldsymbol{p})\rangle\,, \tag{2}$$

where $\boldsymbol{K}$ is the total momentum of the interacting pair, $\boldsymbol{K} = \boldsymbol{k} + \boldsymbol{p}$, and

$$e_p = \frac{p^2}{2m} + U(p)\,, \tag{3}$$

the sp energy defined in terms of an auxiliary field U. The nucleon mass m is taken as the average of proton and neutron masses. In the BHF approximation the sp potential is given by the on-shell mass operator,

$$U(k) = \mathsf{Re}\,M(k;e_k)\,, \tag{4}$$

self-consistency requirement which can be achieved iteratively. In the continuous choice this condition is imposed at all momenta k [13].

In momentum representation the BHF equation takes the explicit form

$$\langle\boldsymbol{\kappa}'|g_{\boldsymbol{K}}(\omega)|\boldsymbol{\kappa}\rangle = \langle\boldsymbol{\kappa}'|v\,|\boldsymbol{\kappa}\rangle + \int \mathrm{d}\boldsymbol{q}\,\langle\boldsymbol{\kappa}'|v\,|\boldsymbol{q}\rangle \times \frac{\Theta(k_+ - k_F)\Theta(k_- - k_F)}{\omega + i\,\eta - \frac{k_+^2}{2m} - \frac{k_-^2}{2m} - \Sigma}\,\langle\boldsymbol{q}|g_{\boldsymbol{K}}(\omega)|\boldsymbol{\kappa}\rangle\,, \tag{5}$$

where Σ accounts for the particle-particle (pp) potential

$$\Sigma(K,q;x) \equiv U(k_+) + U(k_-)\,, \tag{6}$$

with

$$k_\pm^2 = \frac{K^2}{4} + q^2 \pm qKx\,. \tag{7}$$

Here $x = \hat{\boldsymbol{K}}\cdot\hat{\boldsymbol{q}}$, corresponding to the cosine of the angle between $\boldsymbol{K}$ and $\boldsymbol{q}$, with $\boldsymbol{q}$ the relative momentum of intermediate states.

3 Methods

A standard procedure to solve the non-linear system of eqs. (1)–(4) is by iterative feed-backing, where the auxiliary field U is initially unknown. Each cycle begins with the definition of an initial guess for $U(k)$, which allows solving eq. (1) for any ω and K. The series of cycles may be started with $U_0(k) = 0$, to obtain all g-matrix elements needed for the evaluation of M in eq. (2). The real part of M defines a new sp field, U_1, which becomes the guess for a new cycle. The procedure is repeated until differences between consecutive solutions for U meet some convergence criterion. Although this self-consistent scheme works well at normal densities, convergence becomes more difficult as k_F diminishes below $\sim 0.8\,\mathrm{fm}^{-1}$, feature manifested by instabilities in the evaluation of the on-shell mass operator. To attenuate these instabilities we cite refs. [14], for example, where self-consistency at low densities was reached by reducing the number of mesh points for the Fermi-motion integral in eq. (2). With such numerical compromise it was possible to attenuate sudden fluctuations of the integrand, which at the time of the work had no identifiable cause.

These solutions are used to calculate the nucleon-nucleon (NN) effective interaction, *i.e.* the off-shell g matrix, to evaluate momentum-space optical model potentials for nucleon scattering off nuclei.

Aiming to obtain genuine self-consistent solutions for the sp mean fields over a wide density regime, particularly at low densities, a refinement of numerical techniques becomes crucial to control instabilities during the iterative process. In the following we describe the most relevant constructions toward this end.

3.1 Multiple roots

To solve eq. (5) we take the angular average of the energy denominator,

$$\bar{\Sigma}(K,q) = \frac{1}{\Delta}\int_0^{\Delta} [U(k_+) + U(k_-)]\,\mathrm{d}x\,, \tag{8}$$

where $\Delta = \Delta(K,q) = \min\{1, \max[0, (K^2/4 + q^2 - k_F^2)/qK]\}$. Additionally, if the Pauli blocking operator is angle-averaged the multi-channel coupling among different total angular momentum states become disentangled. In ref. [15] this is referred to as ratio-of-average approximation, which in this study constitutes a starting point. After partial wave expansion, eq. (1) for uncoupled channels reads

$$g(k',k;\omega) = v(k',k) + \frac{2}{\pi}\int_0^{\infty} q^2\,\mathrm{d}q\, v(k',q) \times \frac{\Delta(K,q)}{\omega + i\eta - E(K,q)}\, g(q,k;\omega)\,, \tag{9}$$

where

$$E(K,q) = \frac{K^2}{4m} + \frac{q^2}{m} + \bar{\Sigma}(K,q)\,. \tag{10}$$

A similar equation is obtained in the case of coupled states. The above integral equation can be solved numerically with the use of numerical quadrature and matrix inversion. However, caution is called for in the treatment of the zeros of the energy denominator. Indeed, the fact that $e_k = k^2/2m + U(k)$ is a growing function in k does not necessarily imply the same trend for the two-particle energy $E(K,q)$. Hence, more than one root in the energy denominator of eq. (9) cannot be ruled out.

To clarify this point consider the angle-averaged potential $\bar{\Sigma}(K,q)$ in eq. (8) evaluated using a two-point Gaussian quadrature. Thus

$$E(K,q) \approx \frac{K^2}{4m} + \frac{q^2}{m} + U(p_+) + U(p_-)\,, \tag{11}$$

where $p_\pm = (K^2/4 + q^2 \pm Kq/\sqrt{3})^{1/2}$. Single zeros (or none) in $E(K,q) - \omega$ are guaranteed if $E(K,q)$ is an ever growing function in q, namely $\partial E(K,q)/\partial q > 0$. Hence,

$$\frac{2q}{m} + q\left[\frac{U'(p_+)}{p_+} + \frac{U'(p_-)}{p_-}\right] + \frac{K}{2\sqrt{3}}\left[\frac{U'(p_+)}{p_+} - \frac{U'(p_-)}{p_-}\right] > 0\,, \tag{12}$$

where U' stands for derivative of U with respect to its argument. Assuming $U'(k)$ positive for all k, the validity of the above inequality depends on the sign of the third term. Only if $U(k)$ is quadratic in k would the above inequality be met, which is not the case in actual solutions.

Therefore, even if the genuine sp self-consistent fields result as monotonic functions in the momentum space, multiple roots cannot be ruled out in the energy denominator of the propagator. This aspect, in the context of the integral equation for the g matrix, can be handled as outlined in appendix A.

3.2 Fermi-motion integrals

The evaluation of the sp fields, $U(k) = \mathsf{Re}\, M(k, e_k)$, involves the summation of on-shell g-matrix elements while keeping the momentum of one of the particles below the Fermi surface. Explicitly,

$$M(k,e_k) = \sum_\alpha n_\alpha \int_0^{k_F} p^2 \mathrm{d}p \times \int_{-1}^{1} \mathrm{d}u\, g^\alpha_{\boldsymbol{k}+\boldsymbol{p}}\left(\frac{|\boldsymbol{k}-\boldsymbol{p}|}{2}, \frac{|\boldsymbol{k}-\boldsymbol{p}|}{2}; \omega\right). \tag{13}$$

Here $u = \hat{\boldsymbol{k}}\cdot\hat{\boldsymbol{p}}$, the energy ω is evaluated on-shell ($\omega = e_k + e_p$), α denotes spin, isospin and angular momentum states, and n_α accounts for their degeneracy and for geometric factors.

For most NN states the integration within the Fermi sphere involves well behaved integrands, as given by the on-shell g. However, extra measures becomes unavoidable when considering the ${}^1S_0$ and ${}^3SD_1$ channels. This is because during the evaluation of the momentum integral in eq. (13), exceedingly large g-matrix elements may occur, stemming from NN bound states in these S and D channels. Indeed, any matrix element with starting energy near these bound states will lead to large contributions. To illustrate the occurrence of these states, let us define

$$D_\alpha(K;\omega) \equiv \det[1 - v_\alpha \Lambda_K(\omega)]\,, \tag{14}$$

with $\Lambda_K(\omega)$ the pp propagator in eq. (9) and α denoting a particular NN channel. In fig. 1 we plot D_α for ${}^1S_0$ (thin curves) and ${}^3SD_1$ (thick curves) channels as a function of $(\omega - \omega_{\mathrm{th}})$, with ω_{th} the threshold energy allowed by Pauli blocking. For this example we have chosen $k_F = 0.6\,\mathrm{fm}^{-1}$. Solid, long- and short-dashed curves correspond to total pair momenta $K = 0$, 0.05 and $0.1\,\mathrm{fm}^{-1}$, respectively. A singularity of $g_K(\omega)$ in channel α is identified by the zero of $D_\alpha(K;\omega)$. As observed, the deuteron channel exhibits bound states in all three cases, while for the ${}^1S_0$ channel they occur over a narrower interval in ω. Hence, if during the evaluation of the $\mathrm{d}p\,\mathrm{d}u$ integrals in eq. (13) a configuration of total momentum K and starting energy ω happens to be near (or at) one of these singular points, large (or undefined) contributions become unavoidable. This feature becomes a major source of numerical instabilities if not handled properly.

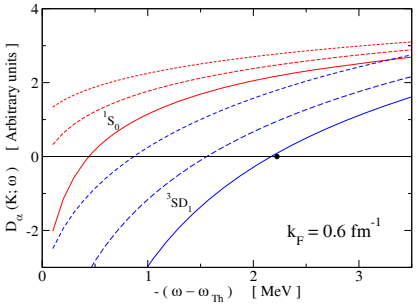

Fig. 1. Determinant $D_\alpha(K,\omega)$ as a function of ω for ${}^1S_0$ (thin curves) and ${}^3SD_1$ (thick curves) channels, at $k_F = 0.6\,\mathrm{fm}^{-1}$. Solid, long- and short-dashed curves indicate $K = 0$, 0.05 and $0.1\,\mathrm{fm}^{-1}$, respectively. The circle at 2.224 MeV denotes deuteron binding in free space.

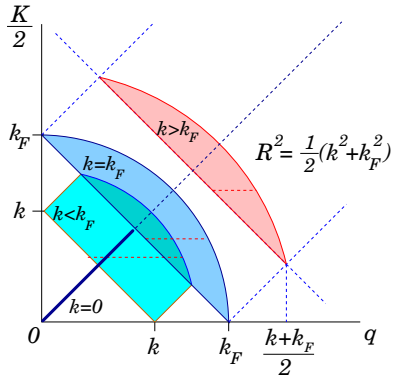

Fig. 2. Domains of integration in the $(\frac{1}{2}K, q)$-plane for different values of k relative to k_F. The radii R of the arcs satisfy $R^2 = (k^2 + k_F^2)/2$. The slopes of the straight lines are ± 1.

To evaluate the mass operator we use the alternative set of variables q and K defined by [16]

$$q = \frac{1}{2}(k^2 + p^2 - 2kpu)^{1/2}\,, \tag{15a}$$

$$K = (k^2 + p^2 + 2kpu)^{1/2}\,. \tag{15b}$$

Thus, $p^2\mathrm{d}p\,\mathrm{d}u = (2Kq/k)\mathrm{d}K\,\mathrm{d}q$. Therefore the on-shell mass operator, eq. (13), is now expressed as

$$M(k,e_k) = \sum_\alpha n_\alpha \int_{K_{\min}}^{K_{\max}} K\,\mathrm{d}K \int_{q_{\min}}^{q_{\max}} \frac{2q\,\mathrm{d}q}{k}\, g_K^\alpha(q,q;\omega). \tag{16}$$

To be consistent with the angle-averaged pp energy, the starting energy $\omega = e_p + e_k$ is evaluated according to eq. (10). With this set of integration variables, for given k_F, k and K, the limits of integration on q become

$$q_{\min} = \left|k - \frac{1}{2}K\right|\,,$$

$$q_{\max} = \begin{cases} \min\left\{k + \frac{1}{2}, (R^2 - \frac{1}{4}K^2)^{1/2}\right\}\,, & \text{for } k \le k_F\,, \\ \left(R^2 - \frac{1}{4}K^2\right)^{1/2}\,, & \text{for } k > k_F\,, \end{cases}$$

where $R^2 = \frac{1}{2}(k^2 + k_F^2)$. In the case of K, the integration ranges from $K_{\min} = \max\{0, k - k_F\}$, up to $K_{\max} = k + k_F$. In fig. 2 we illustrate the four possible shapes in the $(\frac{1}{2}K, q)$-plane where the integral on $\mathrm{d}K\,\mathrm{d}q$ takes place, depending on k relative to k_F.

The above choice of coordinates facilitates tracking and control of dinucleon singularities. Indeed, for constant K the eigenenergy ω_K^* of an eventual dinucleon bound-state pole remains unchanged while the integration on q takes place. Additionally, considering the spectral representation of g when bound states occur [17], its behavior for ω near the energy of the bound state becomes

$$g_K^\alpha(\omega) \sim \frac{vQ|\psi_K^\alpha\rangle\langle\psi_K^\alpha|Qv}{\omega - \omega_K^*}\,, \tag{17}$$

with $|\psi_K^\alpha\rangle$ the eigenfunction at the pole, v the bare potential in the corresponding channel, and Q the Pauli blocking operator. This analytic property allows us to safely state that the mass operator, expressed as an integral over momenta of g with isolated singularities, should be finite. The rationale behind this statement is that if simple poles occur, the integration over q of the singular part of g in eq. (16) reduces to

$$\mathcal{I} = \int_{q_{\min}}^{q_{\max}} \frac{2q\,\mathrm{d}q}{k}\, \frac{|\langle q|vQ|\psi_K^\alpha\rangle|^2}{E(K,q) - \omega_K^*}\,. \tag{18}$$

Note that the numerator is bound. Expanding the denominator to first order in q around its zero, which we assume inside the interval of integration, the contribution around the singularity can be reduced to the form $\int_{-\delta}^{\delta} \frac{\mathrm{d}x}{x}$, which becomes finite. Therefore, integrals over momenta of the g matrix featuring dinucleon poles are not only finite but should be feasible. In actual calculations these singularities are controlled with the regularization

$$g(\omega) \to g(\omega) \times \frac{(\Delta\omega)^2}{(\Delta\omega)^2 + \eta^2}\,, \tag{19}$$

where $\Delta\omega = \omega - \omega_K^*$, and η is an infinitesimal. In this way contributions too close to the pole, namely $\Delta\omega/\eta \to 0$, become attenuated. On the other hand g is practically unchanged whenever $|\Delta\omega|/\eta \gg 1$. In the actual implementation of this technique we have used $\eta = 0.1\,\mathrm{MeV}$. These considerations in the handling of ${}^1S_0$ and deuteron bound states render a much needed stability in the evaluation of the Fermi-motion integrals, which otherwise become uncontrollable.

Another aspect of particular relevance in the evaluation of M in eq. (16) is the quadrature method to be used. Two elements enter into consideration here. On the one hand it is the varying range of integration along q for fixed K (see fig. 2); on the other hand, it is the presence of bound states responsible for steep variations of g. These features combined make inadequate the use of Gaussian-type quadratures designed for smooth integrands.

Aiming to a reliable precision in the evaluation of Fermi-motion integrals we have resorted to an adaptive trapezoidal quadrature considering gradually $2, 3, 5, \ldots, (2^n + 1)$ knots. The scheme, described in

appendix B, is first applied to the (innermost) q quadrature and then to the integration over K. The sequence is interrupted once the difference between two consecutive evaluations is bound to 2%. Given that in many cases the integrand is smooth and the spacing between consecutive knots diminishes exponentially, this criterion provides an overall accuracy in the sp fields of the order of 0.5%. We have limited n to eight, leading to 255 trapezoids over a given interval. Self-consistency of the calculated $U(k)$ is achieved when the maximum fluctuations of $U(k_i)$ over three consecutive cycles do not exceed 0.04 MeV, condition imposed at all k_i where U is evaluated. In this work we have used $k \leq 5.5\,\mathrm{fm}^{-1}$.

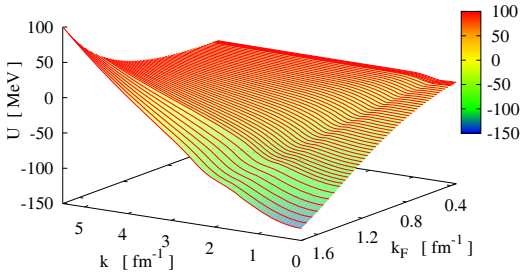

Fig. 3. Surface plot for U_{II} as a function of k and k_F, in the case $k_F \geq 0.35\,\mathrm{fm}^{-1}$.

4 Results

Self-consistent solutions for $U(k)$ were obtained in the range $0 < k_F \leq 1.75\,\mathrm{fm}^{-1}$ using the Argonne v_{18} bare internucleon potential [18]. We have included all NN partial waves up to $J = 7\hbar$, the total angular momentum. This criterion was maintained at all densities in order to cross-check our findings near the saturation point, in addition to rule out any subtle variation of the calculated observables as caused by a discrete (sudden) change in the number of partial waves taken into account. With these specifications and the numerical considerations described in the previous section, each cycle at which U is calculated involves between 10^5 and 10^6 matrix inversion operations, depending on the sharpness of the integrand.

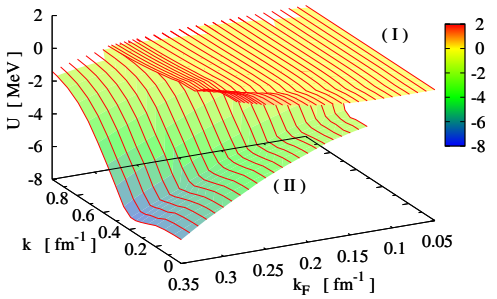

Fig. 4. Surface plots for U_I and U_{II} as functions of k and k_F, when $k_F \leq 0.35\,\mathrm{fm}^{-1}$.

4.1 Self-consistent solutions

Usually the search for self-consistent solutions to the sp field by iterative feedback is stable enough to reach unique solutions, even starting out with zero field. We find this to be the case when the Fermi momentum is near and above $0.35\,\mathrm{fm}^{-1}$. The issue becomes more subtle at lower densities, where the iterative process yields ill-behaved solutions. This fact has led us to adopt different strategies for $0 < k_F < 0.35\,\mathrm{fm}^{-1}$ and $k_F \geq 0.35\,\mathrm{fm}^{-1}$. In the second case we have found unique self-consistent solutions at Fermi momenta $k_F = 0.35(0.05)1.75\,\mathrm{fm}^{-1}$, following the usual iterative procedures.

In contrast to this upper range, searches in the interval $0 < k_F < 0.35\,\mathrm{fm}^{-1}$, required a specific strategy due to the fact that two different self-consistent solutions could be obtained for the same value of k_F. These two genuine solutions meeting self-consistency will be referred to as *coexisting solutions*. To proceed systematically, a first class of solutions was obtained with ascending k_F, in steps of $\Delta k_F = 0.01\,\mathrm{fm}^{-1}$. At each k_F, the self-consistent loop starts with an $U(k)$ borrowed from the converged solution at the previous k_F. In this way, starting at $k_F = 0.01\,\mathrm{fm}^{-1}$, we obtain a class of self-consistent solutions characterized by a monotonically increasing binding energy per nucleon, B/A, as a function of k_F. We denote this class of solutions as $U_I = \{U_{k_F} \mid 0 \leq k_F \leq k_\beta\}$, with k_β the maximum (critical) Fermi momentum at which self-consistency is achievable in ascending order. To resolve k_β, self-consistent solutions were explored with increasing k_F in steps Δk_F as small as $0.001\,\mathrm{fm}^{-1}$, obtaining $k_\beta = 0.285\,\mathrm{fm}^{-1}$. Beyond this point the iteration loops indefinitely, with fluctuations in $U(k)$ unable to settle below 0.04 MeV. A more refined characterization of the solutions near and beyond k_β may require a more specific approach.

A similar procedure was adopted for decreasing k_F, starting from the converged solution at $k_F = 0.35\,\mathrm{fm}^{-1}$ and going down in steps of $0.01\,\mathrm{fm}^{-1}$. As in the previous case, the continuity of B/A is monitored and we seek the minimum critical value of k_F, denoted by k_α, at which self-consistency is reachable. This second class of solutions is denoted $U_{II} = \{U_{k_F} \mid k_F \geq k_\alpha\}$. We obtain $k_\alpha = 0.130\,\mathrm{fm}^{-1}$, with a resolution of $0.01\,\mathrm{fm}^{-1}$.

In fig. 3 we show a surface plot of the calculated self-consistent solutions U_{II}, as functions of k and the Fermi momentum k_F, with $k_F \geq 0.35\,\mathrm{fm}^{-1}$. In general terms they follow the same trend as those reported elsewhere [13], with $U(k)$ negative at $k = 0$, growing as k increases.

In fig. 4 we show surface plots for the self-consistent fields $U(k)$ for solutions I and II in the range $0.05\,\mathrm{fm}^{-1} \leq k_F \leq 0.35\,\mathrm{fm}^{-1}$. These solutions define distinct surfaces at densities corresponding to $k_\alpha \leq k_F \leq k_\beta$. The upper sheet, representing U_I, features a moderate repulsion at $k = 0$, with a shallow ditch in the vicinity of $k \sim 4k_F/3$. On the other hand the sheet for U_{II} starts with negative

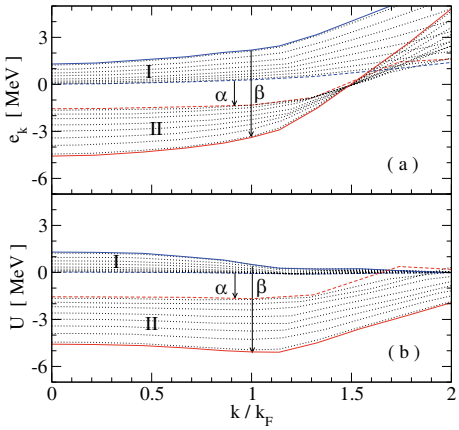

Fig. 5. Single-particle energies (a) and potentials (b) in the coexistence region as functions of k/k_F. Dashed and solid curves represent solutions for k_F at k_α and k_β, respectively.

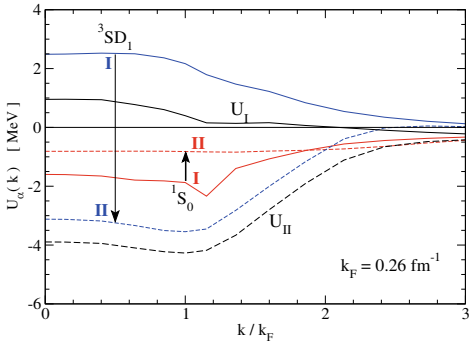

Fig. 6. $^3SD_1$ and $^1S_0$ partial contributions to the total sp potential $U(k)$ as functions of k/k_F at $k_F = 0.26\,\mathrm{fm}^{-1}$. Solid and dashed curves represent phases I and II, respectively.

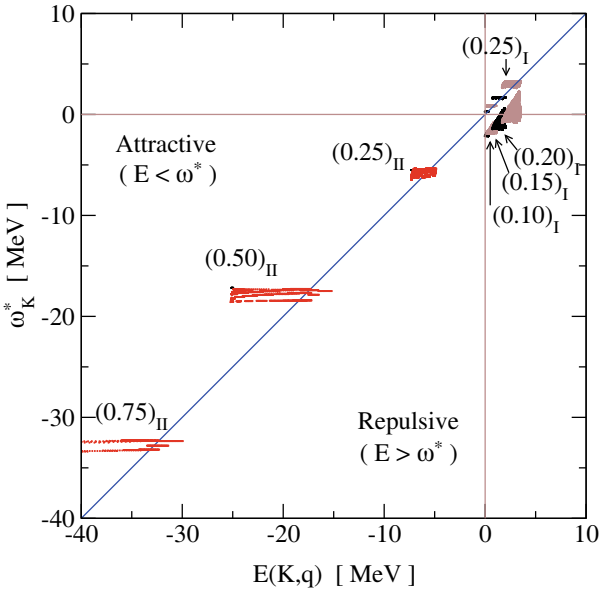

Fig. 7. Location of poles ω_K^* (if detected) and pair energy ($E = e_p + e_k$), upon evaluation of $U(k)$ for $k \lesssim 1.2k_F$. The numbers in parenthesis represent k_F (in fm^{-1} units), with the subscript referring to phase I or II. Variations of (K, q) are in correspondence with domains shown in fig. 2.

mean fields at $k = 0$, showing a moderate decrease up to $k \sim k_F$ and then followed by a steep increase to reach $U(k) \to 0$. In both cases the slope of the self-consistent fields become negative at the Fermi surface, feature responsible for nucleon effective masses greater than the bare nucleon mass, to be discussed ahead.

A closer view of the coexisting solutions is presented in fig. 5, where in panel (a) we plot sp energies as functions of the ratio k/k_F in the coexistence region, and in panel (b) the corresponding sp potentials. Dashed and solid curves represent solutions for $k_F = k_\alpha$, and $k_F = k_\beta$, respectively. Dotted curves represent consecutive solutions for $k_F = 0.14(0.02)0.28\,\mathrm{fm}^{-1}$. Vertical arrows connect coexisting solutions at k_α and k_β, respectively. The difference between Fermi energies of solutions I and II is 1.6 MeV at k_α, and 5.6 MeV at k_β. We also notice that none of the solutions for $U(k)$ (lower panel) exhibits a parabolic behavior in the whole momentum range. As a matter of fact the slope of $U(k)$ for solution I exhibits a sudden increase from negative to near-zero at $k/k_F \approx 1.15$, while for solution II the increase goes from near-zero to positive slope. These features rule out the validity of the effective mass approximation at low densities.

The disclosure of the two distinct phases I and II for the sp spectrum constitutes an unexpected outcome of the calculations we have performed for nuclear matter in normal state. To gain insight into possible causes behind this behavior, in fig. 6 we plot the total sp potentials U_I and U_{II}, together with the partial contributions from $^3SD_1$ and $^1S_0$ channels. Solid and dashed curves represent solutions in phase I and II, respectively. In this illustration we have selected $k_F = 0.26\,\mathrm{fm}^{-1}$, a Fermi momentum reasonably close to k_β but not at the edge of the overlap. The most prominent difference between phases I and II appears in the deuteron channel, passing from a correlated Fermi gas (FG) behavior in phase I to an attractive (condensing) state in phase II, with an energy decrease of about 6 MeV near the Fermi surface ($k/k_F \approx 1$). This is in contrast with the moderate increase, by about 1 MeV, observed in the $^1S_0$ channel. This feature points to the deuteron as the driving constituent responsible for the occurrence of phase II beyond k_α.

The above comments are reinforced if we track $^1S_0$ and $^3SD_1$ bound state occurrences while performing the Fermi motion integration (see eq. (2)) through the (K, q) domains displayed in fig. 2. In fig. 7 each dot represents the energy of a detected pole, $\omega_K^* < \omega_{th}$, and the set of starting energies $E = e_p + e_k$, of the energy denominator in eq. (18) when integration on q is performed. These dots are collected when $U(k)$ is evaluated for discrete values of $k \lesssim 1.2k_F$, typical momentum below which poles are detected while performing Fermi-motion integrals. Note that $E(K, q) = e_p + e_k$, when angular average is applied. Dots appear separated as a result of the fact that (adaptive) quadratures are used for both dq and dK integrations. In fig. 7 a few selected values of k_F, indicated with numbers but omitting fm^{-1} units, are chosen for clarity. Clusters of

dots in the form of "islands" displayed in the upper part of the panel, where $E(K,q) > 0$, correspond to phase I. Out of these clusters, the ones leaning to the right-hand side with respect to the diagonal correspond to the $^3SD_1$ channel (subject to existence of a pole). Similarly, the clusters in phase I being crossed by the diagonal line correspond to the $^1S_0$ channel. From eq. (18) we infer positive (repulsive) contributions if $E(K,q) > \omega^*_K$, corresponding to the sector to the right-hand side of the diagonal. Conversely, attractive contributions stemming from dinucleons are located in the left-hand side of the diagonal. In this "$E-\omega$" plot, the closer a dot is from the diagonal, the stronger is the associated contribution in the respective channel. The actual strength of the contribution will depend on the principal value of the pole. In fig. 7 the clusters shown for phase II correspond to the $^3SD_1$ channel (very few or no poles are detected in the $^1S_0$ channel), which appear crossed by the diagonal but leaning toward the region $E < \omega^*$. This indicates dominance of negative contributions in the $^3SD_1$ channel, in contrast to phase I where clusters in same channel lean toward positive contribution, *i.e.* repulsive.

The strategy we have adopted to obtain self-consistent solutions, starting out iterative loops with a converged solution at a nearby k_F, has proven essential to elucidate the coexisting solutions. Actually if such a measure was not taken the calculated $U(k)$ might exhibit piecewise zigzagging instabilities, preventing any relaxation toward convergence. In the case of solution I, successive solutions were obtained with increasing k_F up to k_β. When the solution at $k_F = k_\beta$ was used as starting guess for $k_F = k_\beta + \delta$, with δ some small increment, the requirement we have established for stable solutions could not be met after sixty iterative loops. However, if the increment is large enough the self-consistent solution settles over that of U_{II}. An analogous process is followed to obtain solution II, but generating solutions with decreasing k_F down to k_α. Here again, the use of $U(k)$ at k_α to start iterations for $k_F = k_\alpha - \delta$, would not relax if δ were small and positive, but it would settle over U_I if δ were large enough. In this respect, the procedure to obtain the solutions in the coexistence interval $[k_\alpha, k_\beta]$ resembles that of hysteresis.

The procedure described above was repeated all through the range $k_F \lesssim 0.3\,\mathrm{fm}^{-1}$, assuming valid the effective mass approximation while solving eqs. (1)-(4) subject to dinucleon bound state occurrences and self-consistency. We have been able to identify phase I, though over a more limited range, when the quadratic approximation of $U(k)$ is imposed over the range $0 \le k \le 2k_F$. However, solutions for phase II become unstable, preventing actual self-consistency. An specific study on merits and shortcomings of the effective mass approximation goes beyond the scope of this work.

4.1.1 Binding energy

The fact that two different solutions for $U(k)$ satisfy self-consistency at a given Fermi momentum between k_α and k_β, implies two accessible sp states for nucleons in the medium. If these were the only degrees of freedom of the system, then solution II would be the one accountable for the ground state. However, pairing correlations beyond normal BHF would change the scenario, an aspect that needs to be investigated within a more general framework [19]. Having these shortcomings in mind, we have proceeded to evaluate the binding energies per nucleon of the system considering phases I and II, separately. This simplifying assumption would help us to set bounds to the results.

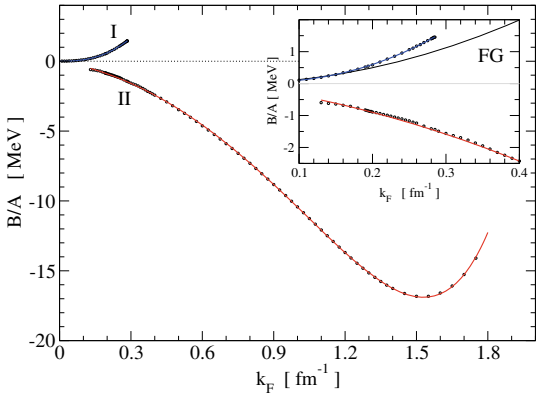

Fig. 8. Calculated B/A for symmetric nuclear matter as a function of the Fermi momentum k_F. Continuous curves represent the parametrization defined by eqs. (21). Small circles denote actual results. Inset shows a close up at low densities, including a free Fermi gas.

In fig. 8 we plot the binding energy per nucleon for symmetric nuclear matter, B_I/A and B_{II}/A, as obtained from solutions U_I and U_{II}, respectively. Here each small dot denotes an actual calculation, while the continuous curves represent suitable parametrizations. We note that the two solutions exhibit distinct behaviors as functions of k_F in their respective domains, without intercepting each other in the range $[k_\alpha, k_\beta]$. While solution I resembles a correlated FG in metastable state, solution II represents a condensed medium featuring a minimum at the point of nuclear saturation. From the inset for low densities we also note that solution I departs from an uncorrelated FG above k_α, the Fermi momentum where solution II begins. This departure features a moderate repulsiveness relative to a free FG.

To facilitate the analysis of solutions I and II we have found simple parametrizations of the mean potential energy

$$u(k_F) \equiv \frac{3}{k_F^3}\int_0^{k_F} k^2 \mathrm{d}k\, U(k)\,. \tag{20}$$

Specifically,

$$u_I(x) = a_2(x/a)^2 + a_3(x/a)^3 + a_6(x/a)^6\,, \tag{21a}$$
$$u_{II}(x) = b_1(x/b) + b_2(x/b)^2 + b_7(x/b)^7\,, \tag{21b}$$

with $a = 0.3\,\mathrm{fm}^{-1}$, and $b = 1.53\,\mathrm{fm}^{-1}$. These constructions lead to accurate representations of the calculated binding

Table 1. Best-fit coefficients for $u(k_F)$.

p	a_p (MeV)	p	b_p (MeV)
2	−1.25	1	−8.91
3	2.69	2	−94.89
6	−0.37	7	11.91

energy per nucleon

$$B_i/A = \frac{3}{10}\frac{k_F^2}{m} + \frac{1}{2}u_i(k_F)\,, \qquad (22)$$

with $i = I$ and II. The coefficients a_p and b_p, summarized in table 1, were obtained from least-square fitting procedures for the calculated B_i/A values as functions of k_F. The standard deviations associated with each set of coefficients are 0.01 MeV and 0.06 MeV, respectively. In the case of solution B_{II}/A we obtain a saturation energy of −16.8 MeV at $k_F = 1.53\,\mathrm{fm}^{-1}$, with an incompressibility $K_\infty = 213$ MeV.

The coexistence of solutions I and II in the range $k_\alpha \le k_F \le k_\beta$ define three distinct regimes according to k_F, namely: i) a diluted phase in the form of an interacting FG up to k_α; ii) a mixed phase with coexisting sp states between k_α and k_β; and iii) a condensing phase above k_β. The low-density behavior of B/A in phase I, featuring a repulsive FG, points to dominance of the kinetic contribution over its interaction term. Being this the case, if no condensation takes place, the gas behavior up to $k_F \sim 0.13\,\mathrm{fm}^{-1}$ ($\rho \sim 10^{-4}\,\mathrm{fm}^{-3}$), prevents homogeneous symmetric nuclear matter in normal state from spontaneous collapse. As we shall see later, this repulsiveness gets greately attenuated if the sp momentum distribution accounts for pairing correlations.

A survey of available literature have resulted in scarce information on zero-temperature and low-density behavior of symmetric nuclear matter ($k_F \lesssim 0.4\,\mathrm{fm}^{-1}$, or $\rho \lesssim 0.004\,\mathrm{fm}^{-3}$) when the bare NN interaction is used. In ref. [20] for instance, the authors have made explicit the fact that a polynomial extrapolation is used for densities below $0.02\,\mathrm{fm}^{-3}$ (*i.e.* $k_F < 0.67\,\mathrm{fm}^{-1}$). Extrapolations of similar nature, roughly from the same density, have been made in refs. [21,22] in the context of density-dependent effective interactions based on BHF model and applied to nucleon-nucleus scattering. In a recent publication [23] aimed to the study of the phase structure of symmetric nuclear matter in the extended Nambu-Jona-Lasinio model, fig. 1 for B/A as a function of the density suggests FG behavior at $\rho \lesssim 0.007\,\mathrm{fm}^{-3}$, although no comments are made by the authors on this feature.

4.1.2 Effective masses and dinucleon binding

In this section we examine the density dependence of the effective mass and dinucleon binding energies associated to each phase in normal state. To this end, we show in panel (a) of fig. 9 the total effective mass relative to the bare nucleon mass, m^*/m, as a function of the Fermi momentum. Phase-I results are plotted up to k_β, while results for phase II appear for $k_F \ge k_\alpha$. In this case we evaluate

$$\frac{m^*}{m} = \left[1 + \frac{m}{k}\frac{\partial U(k)}{\partial k}\right]^{-1}\,, \qquad (23)$$

at $k = k_F$. In panel (b) we plot dinucleon binding energies in states $^3SD_1$ (circles) and $^1S_0$ (squares), in units of deuteron binding in free space, $E_d = -2.224$ MeV. The dinucleon binding energy E is given by

$$E = \omega - \omega_{\rm th}\,,$$

with ω the eigenenergy (see eq. (14)) and $\omega_{\rm th}$ the pp energy at the Fermi surface. Here we restrict to cases where $K = 0$, *i.e.* pairs with no translational motion. For reference purposes, in panel (c) we plot again the binding energy per nucleon associated with solutions I and II. The upper scale denotes density, $\rho = 2k_F^3/3\pi^2$. We first observe that m^*/m for solution I grows monotonically with increasing k_F, reaching a maximum $m^*/m \approx 3$, close to the upper edge of the coexistence interval (k_β). In turn, m^*/m for solution II starts out near unity at k_α, reaching a maximum $m^*/m \approx 1.8$, at $k_F = 0.55\,\mathrm{fm}^{-1}$. Beyond $k_F = 0.9\,\mathrm{fm}^{-1}$, m^*/m decreases monotonically, taking values from 0.88 to 0.79 for Fermi momenta from 1.3 to $1.5\,\mathrm{fm}^{-1}$, respectively, consistent with quotes found in the literature. In the domain of coexistence the two solutions yield dressed nucleons with distinct effective masses, reaching values as high as $m^*/m \approx 3$, for solution I and $m^*/m \approx 1$, for solution II.

Panel (b) of fig. 9 shows qualitative similarities between deuteron and $^1S_0$ binding energies, although differences point to weaker binding in the case of the $^1S_0$

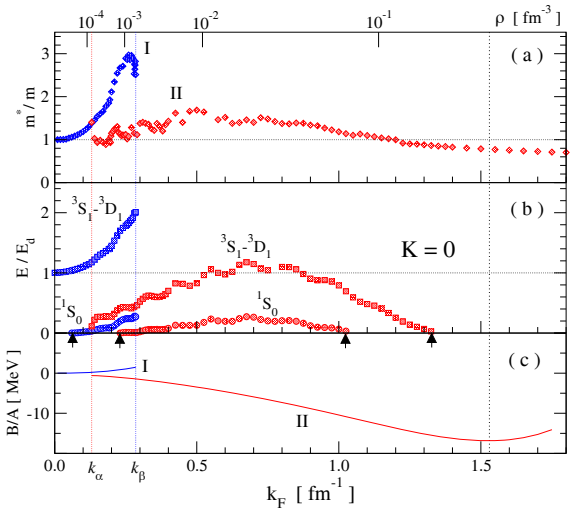

Fig. 9. Effective mass relative to the bare mass (a); dinucleon binding energies relative to $E_d = 2.224$ MeV, for $K = 0$ (b); and binding energy per nucleon (c), as functions of k_F. The upper scale denotes nucleon density ρ. The rightmost dotted line is drawn at saturation ($k_F = 1.53\,\mathrm{fm}^{-1}$). Arrows in panel (b) denote loci where dinucleons get dissolved.

channel. Solution I for deuteron pairs shows increasing binding energy as the density grows up to k_β, reaching up to twice that in free space. The same solution but for $^1S_0$ state exhibits increasing binding up to nearly $0.3\,E_d$, although no bound state is found in this channel for k_F below $0.06\,\mathrm{fm}^{-1}$ (Mott transition). In the case of solution II, deuterons pairs are found for $k_F \geq k_\alpha$, but get dissolved beyond $k_F \approx 1.325\,\mathrm{fm}^{-1}$. In turn, $^1S_0$ pairs appear over a narrower range in k_F: 0.23–1.05 fm^{-1}. The strongest bindings are $E/E_d \approx 1.2$ and 0.3, for $^3SD_1$ and $^1S_0$ pairs, respectively. These maxima occur at $k_F \approx 0.7\,\mathrm{fm}^{-1}$. We also notice that the $^1S_0$ and $^3SD_1$ binding energies tied with solution II display shallow extrema. These oscillating patterns are in contradistinction with the smooth behavior displayed over k_F by conventional S and D solutions of pairing gap equations in nuclear matter [24]. We have found no interpretation as to why such pairing gaps and dinucleon binding energies, two closely related properties, differ in their patterns over k_F.

A simple argument of plausibility to admit effective masses greater than bare masses in a very diluted medium comes from considering two nucleons interacting *via* an attractive square well. If the depth of the potential is V_0 and its radius is R, then the condition to hold at least one bound state is $mV_0R^2 > \pi^2/4$. In the context of two interacting neutrons in free space this condition should be regarded as barely missed, as inferred from the low-energy behavior of the phase shifts in the $^1S_0$ channel and scattering length $a_{nn} = -18.5\,\mathrm{fm}$. If we assume unaffected the bare interaction by the medium, then $^1S_0$ pairs become possible provided m^* increases enough so as to allow $m^*V_0R^2 > \pi^2/4$. This trend is observed in panel (b) of fig. 9, where the Fermi momenta at which $^1S_0$ pairs get unbound are indicated with small black arrows on the horizontal axis. Here $k_F = 0.06$, 0.23 and $1.025\,\mathrm{fm}^{-1}$, corresponding to $m^*/m = 1.06$, 1.25 and 1.15, respectively. For deuterons, instead, bound states occurrences appear in correspondence with $m^* \gtrsim 0.87m$. In this case bound states dissolve near $k_F = 1.325\,\mathrm{fm}^{-1}$. These features were cross-checked for solution I with the aid of a simple computer code applied to a square well potential where the trend of m^*/m in panel (a) of fig. 9 can be reproduced by feeding in E/E_d for the deuteron from panel (b).

4.2 Dinucleons

Singularities of the g matrix on the real axis below the Fermi surface, in the $^1S_0$ and $^3SD_1$ channels, are unequivocal signs for in-medium bound states. The former corresponds to a state with total isospin $T = 1$, leading to three possible NN configurations: proton-proton, proton-neutron and neutron-neutron. The latter ($T = 0$) represents a proton-neutron bound state, *i.e.* deuteron. In this section we explore some features of these Cooper pair-like solutions [25], representing the formation of single pairs in the presence of homogeneous nuclear matter within normal state. These bound states correspond to actual solutions of BHF equation. Whether these objects become true in-medium bound states requires the inclusion of hole-hole propagation [26,27].

4.2.1 Bound states in normal BHF

Let E_b be the eigenenergy corresponding to a bound state of two interacting nucleons in the nuclear medium. Then it can easily be shown [5] that

$$\lim_{\eta\to 0} i\eta g(E_b + i\eta) = vQ|\psi\rangle\langle\psi|Qv\,, \tag{24}$$

with Q the Pauli blocking operator and $|\psi\rangle$ the corresponding eigenstate (dependence on $\boldsymbol{K}$ is implicit). On the other hand, the wave equation associated with eq. (1) when ω matches the eigenenergy E_b reads

$$(\hat{h}_1 + \hat{h}_2 + QvQ)|\psi\rangle = E_b|\psi\rangle\,.$$

In free space, where $(\hat{h}_1 + \hat{h}_2)$ becomes the kinetic energy of the two nucleons and Q the identity, this equation reduces to the Schrödinger equation in stationary state. After projecting in momentum space ($\langle\boldsymbol{q}|$) we obtain for the wave function

$$\langle\boldsymbol{q}|\psi\rangle = \frac{\langle\boldsymbol{q}|QvQ|\psi\rangle}{E_b - e_+ - e_-}\,, \tag{25}$$

where $e_\pm = e(k_\pm)$, consistent with the notation in eq. (7). In the case of pairs without translational motion, where $K = 0$, the numerator reduces to

$$\langle\boldsymbol{q}|QvQ|\psi\rangle = \Theta(q - k_F)\langle\boldsymbol{q}|vQ|\psi\rangle\,. \tag{26}$$

Thus, the wave function can be obtained after $\langle\boldsymbol{q}|vQ|\psi\rangle$ is extracted from eq. (24), a procedure we have achieved numerically solving the BHF equation for small η and extrapolating to $\eta \to 0$. The solution in momentum space is then Fourier transformed to get its coordinate space representation.

4.2.2 Eigenfunctions

As mentioned earlier, wave functions are calculated in momentum space. If $\psi(q)$ denotes the wave function for a bound state of orbital angular momentum L, its coordinate space representation is given by

$$\Psi(r) = \sqrt{\frac{2}{\pi}}\int_{\bar{q}}^{\infty} q^2\,\mathrm{d}q\, j_L(qr)\psi(q)\,. \tag{27}$$

The lower integration bound $\bar{q}$ corresponds to that allowed by Pauli blocking. In what follows we shall consider pairs with their center of mass at rest ($K = 0$), so that $\bar{q} = k_F$.

To achieve reliable precision in the evaluation of $\Psi(r)$ we found it crucial to control the behavior of ψ near the Fermi surface. To this end we constructed auxiliary functions

$$\psi_0(q) = Aq^L \exp[-R(q - k_F)]\,\Theta(q - k_F)\,, \tag{28}$$

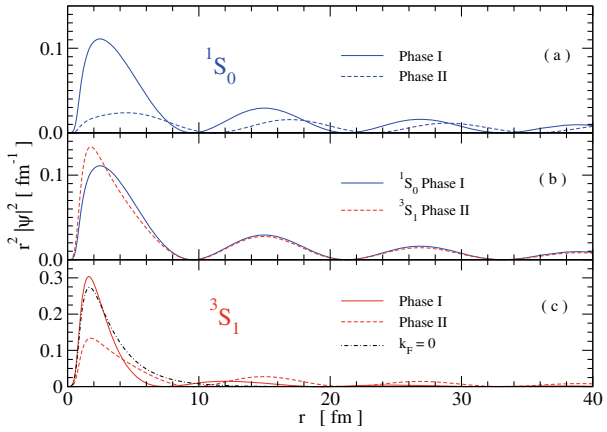

Fig. 10. Radial probability density, $r^2|\Psi(r)|^2$, for in-medium S-wave dinucleon bound state solutions as functions of the relative distance r. Solid (dashed) curves denote solutions for phase I (II) in the case of $k_F = 0.25\,\mathrm{fm}^{-1}$. Panels (a) and (c) show results for channels $^1S_0$ and $^3S_1$, respectively. Panel (b) displays $^1S_0$ and $^3S_1$ bound-state waves in phase I and II, respectively. The dash-dotted curve in panel (c) represents the deuteron in free space.

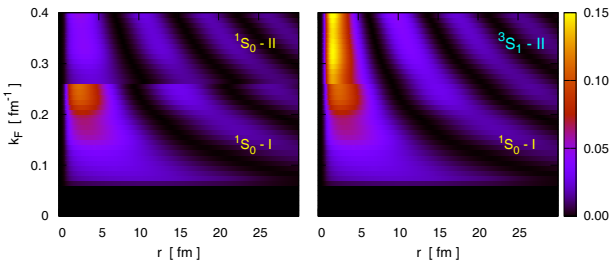

Fig. 11. In-medium S-wave bound-state radial probabilities $r^2|\Psi(r)|^2$ as functions of r and k_F. The left-hand side panel displays $^1S_0$ solutions (phase I, with $k_F \leq 0.26\,\mathrm{fm}^{-1}$, and phase II with $k_F \geq 0.26\,\mathrm{fm}^{-1}$). The right-hand side panel is the same as the left one, but with the $^1S_0$ solution in phase II being replaced by the corresponding $^3S_1$ solution.

with Θ the Heaviside step function to suppress momentum components below the Fermi surface. Parameters A and R are adjusted to match the exact $\psi(q)$ just above the surface, *i.e.* $q \to k_F^+$. With this construction we evaluate

$$\Psi(r) = \sqrt{\frac{2}{\pi}} \int_{k_F}^{\infty} q^2\, \mathrm{d}q\, j_L(qr)(\psi - \psi_0) + \Psi_0(r)\,, \qquad (29)$$

where

$$\Psi_0(r) = \sqrt{\frac{2}{\pi}} \int_{k_F}^{\infty} q^2\, \mathrm{d}q\, j_L(qr)\psi_0(q). \qquad (30)$$

For the latter we proceed analytically, where specific results are presented in appendix C. Integrals are evaluated over finite intervals in r and q, respectively. These intervals are chosen so that

$$\int_0^{R_{\max}} |\Psi(r)|\, r^2 \mathrm{d}r = \int_{k_F}^{q_{\max}} |\psi(q)|^2\, q^2 \mathrm{d}q\,,$$

is met with reasonable precision. Typically $q_{\max} \approx 15\,\mathrm{fm}^{-1}$, whereas $R_{\max}$ could go as high as 1500 fm.

In fig. 10 we plot radial probability densities, $r^2|\Psi(r)|^2$, for S-wave bound states as functions of the relative distance r. These solutions correspond to $k_F = 0.25\,\mathrm{fm}^{-1}$, Fermi momentum where the domains of phases I and II overlap. Panels (a) shows results for the $^1S_0$ channel in phase I (solid curve) and phase II (dashed curve). The same notation is used in panel (c) for the $^3S_1$ channel, where we also include the S-wave deuteron in free space ($k_F = 0$). Panel (b) displays $^1S_0$ and $^3S_1$ bound-state waves in phase I and II, respectively.

We observe that both $^1S_0$ and $^3S_1$ probability densities represent confined systems, exhibiting the same oscillatory behavior of Cooper pair solutions reported in refs. [28,29]. In the case of the $^1S_0$ bound state shown in panel (a) we notice an outward shift of phase-II solution relative to that in phase I. This indicates an enlargement of $^1S_0$ pairs in phase II relative to those in phase I, to be discussed later. The same feature is observed for deuterons in panel (c), where the free-space solution (solid black curve) is included. In this case we observe a similarity between the probability density of deuterons in free space with that of $^1S_0$ pairs in phase I. This suggests that deuterons maintain their size as long as they remain in phase I. These spatial aspects of in-medium dinucleon solutions shall further be discussed in the following section.

In fig. 11 we show contour plots for S-wave radial probabilities $r^2|\Psi(r)|^2$ as functions of the relative distance r and Fermi momentum k_F. The left-hand side panel shows the $^1S_0$ solutions in phase I, with $0 \leq k_F \leq 0.26\,\mathrm{fm}^{-1}$, together with those in phase II for $k_F \geq 0.26\,\mathrm{fm}^{-1}$. In the right-hand side panel the $^1S_0$ solution in phase II has been replaced by the corresponding $^3S_1$ solution. It is interesting to note how the two solutions appear in phase near the boundary $k_F \sim 0.26\,\mathrm{fm}^{-1}$.

4.2.3 Spatial properties

Cooper-like wave functions appear to have unique spatial properties, especially regarding their large size relative to the mean internucleon distance in the nuclear medium. This feature is already suggested in figs. 10 and 11, where the bound-state wave functions are observed to decay slowly. Actually, these wave functions behave as $\sim \cos(k_F r)/r^2$ for large radii, feature which poses convergence difficulties in the actual evaluation of mean radii $r_m \equiv \langle r \rangle$ or root-mean-square (rms) radii $\langle r^2 \rangle^{1/2}$. In momentum space, in turn, we cannot make straightforward use of the customary identity [30] for the mean-square-radius

$$\langle r^2 \rangle = \frac{\int |\Psi_{\mathrm{pair}}(r)|^2 r^4 \mathrm{d}r}{\int |\Psi_{\mathrm{pair}}(r)|^2 r^2 \mathrm{d}r} = \frac{\int_0^{\infty} (\frac{\partial \psi}{\partial q})^2 q^2 \mathrm{d}q}{\int_0^{\infty} \psi^2 q^2 \mathrm{d}q}\,,$$

due to the discontinuity of the wave function $\psi(q)$ at the Fermi surface. Actually, the above identity is valid as long as the wave function is bound in coordinate space, while

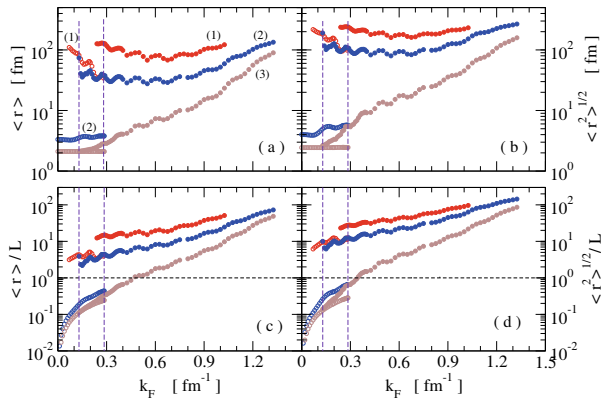

Fig. 12. Mean radii for in-medium $^1S_0$, $^3S_1$ and $^3D_1$ bound states, labeled (1), (2) and (3), respectively, as functions of k_F. Panel (a) and (b) show mean and rms radii, respectively. Panels (c) and (d) show the corresponding quantities but relative to $\rho^{-1/3}$.

in momentum space derivatives are continuous at all momenta. Such is not the case for $\psi(q)$, exhibiting a cut-off below $q = \bar{q}$, as a result of the sharpness of the sp momentum distribution. This cut-off occurs at k_F for pairs with no translational motion ($K = 0$).

To overcome the convergence difficulties posed in coordinate space evaluations, we propose to consider the Laplace transform of the density $r^2|\Psi(r)|^2 \equiv r^2\rho$. This transform reads

$$F(s) = \mathcal{L}\{r^2\rho(r)\} = \int_0^\infty e^{-sr}\,|\Psi(r)|^2 r^2 \mathrm{d}r\,. \qquad (31)$$

Clearly, $F(0) = \mathcal{N}$, the volume integral of the density. The small-s behavior yields

$$F(s) = \mathcal{N}\left(1 - \langle r\rangle\, s + \frac{1}{2}\langle r^2\rangle\, s^2 - \cdots\right),$$

from which we construct the alternative function $f(s)$ given by

$$f(s) \equiv \frac{1}{s}\left[1 - \frac{F(s)}{\mathcal{N}}\right] = \langle r\rangle - \frac{1}{2}\langle r^2\rangle\, s + \cdots\,. \qquad (32)$$

Since $\mathcal{N}$ is finite, $F(s)$ becomes always defined due to the exponential in the integrand. Thus, from an analysis of $f(s)$ at small s we can extract the mean radii $\langle r\rangle$ and the mean-square-radii $\langle r^2\rangle$. A linear regression of eq. (32) for f provides us with accurate fits, with correlations equal to unity out to six significant figures.

In fig. 12 we show results for the calculated mean radii $\langle r\rangle$ and rms radii $\langle r^2\rangle^{1/2}$ as functions of the Fermi momentum k_F. Solutions for states $^1S_0$, $^3S_1$ and $^3D_1$ are labeled as (1), (2) and (3), respectively. Empty and filled symbols denote results for phases I and II, respectively. Upper panels show $\langle r\rangle$ (a) and $\langle r^2\rangle^{1/2}$ (b) in fm units. Lower panels show results for the ratios $\langle r\rangle/L$ (c) and $\langle r^2\rangle^{1/2}/L$ (d), with $L = \rho^{-1/3}$, the mean internucleon separation at density ρ. We note that both mean radii and rms radii for $^1S_0$ pairs (1) are larger than those for deuterons (2 and 3). What is also evident is that S-wave bound states experience a sudden increase of size in the transit from phase I to phase II. The rate of the change is more pronounced for deuterons than for $^1S_0$ pairs. Additionally, observing panels (c) and (d) we note that deuteron bound states in phase I are much smaller than the internucleon separation L, while in phase II they remain bound with sizes several times the internucleon separation.

Another feature worth noting from panel (a) is that the size of deuterons in phase I remain roughly constant as a function of the density ($k_F \leq 0.285\,\mathrm{fm}^{-1}$), with sizes similar to that in free space. In phase II, instead, they become fairly large objects with mean radii above 30 fm. In this respect deuterons change from very compact bosons in phase I to very extended ones in phase II. This is in contrast to $^1S_0$ pairs, where their sizes outpass the internucleon separation in both phases.

4.3 BCS pairing

The occurrence of dinucleon bound states in nuclear medium is closely related with nuclear pairing phenomena, mechanism responsible for the formation of Cooper pairs and emergence of superfluid and superconducting states of matter [1,2]. Hence, it is of interest to explore some immediate implications of phases I and II for the sp potentials in the context of pairing gap equations. To this end we have solved the Bardeen-Cooper-Schrieffer (BCS) gap equations at zero temperature. These gap equations in triplet coupled states lead to coupled equations displaying an explicit angular dependence of the kernel, problem which has been addressed in ref. [31] in the context of pure neutron matter. However, an important simplification to the problem is obtained when the anisotropic kernel is angle averaged [32,33]. Within this approximation the gap functions for states of orbital angular momentum L take the form

$$\Delta_L(k) = -\frac{2}{\pi}\int_0^\infty k'^2\,\mathrm{d}k' \sum_{L'} v_{LL'}(k,k')\,\frac{\Delta_{L'}(k')}{2E(k')}\,, \qquad (33)$$

where the quasiparticle energy reads

$$E(k)^2 = (e_k - \mu)^2 + \Delta(k)^2, \qquad (34)$$

$$\Delta(k)^2 = \sum_L \Delta_L(k)^2\,. \qquad (35)$$

Here μ is the chemical potential and $e_k = k^2/2m + U(k)$, corresponds to the BHF sp spectrum. In this case solutions I and II for $U(k)$ are treated independently, an issue that needs to be re-examined in more realistic calculations. The matrix elements $v_{LL'}(k,k')$ of the bare interaction in a channel of total spin S and isospin T are given by

$$v_{LL'}(k,k') = i^{L-L'}\int_0^\infty r^2\,\mathrm{d}r\, j_L(kr) v_{LL'}(r)\, j_{L'}(k'r)\,. \qquad (36)$$

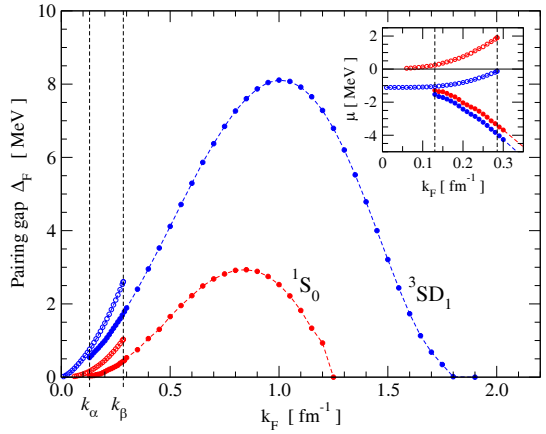

Fig. 13. Energy gap Δ_F as a function of k_F in symmetric nuclear matter for channels $^1S_0$ and $^3SD_1$. Empty and filled symbols denote results for phases I and II, respectively. Inset shows the chemical potential μ as a function of k_F.

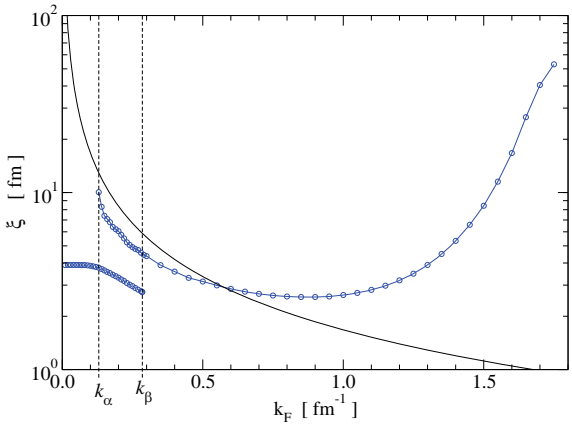

Fig. 14. BCS coherence length in the $^3SD_1$ channel as a function of k_F in symmetric nuclear matter. The solid curve represents the mean internucleon separation $\rho^{-1/3}$.

The corresponding normal (n) and anomalous (κ_L) density distributions are given by

$$n(k) = \frac{1}{2}\left[1 - \frac{e_k - \mu}{E(k)}\right], \quad \kappa_L(k) = \frac{\Delta_L(k)}{2E(k)}, \qquad (37)$$

respectively. Self-consistency for the chemical potential is imposed through

$$\rho = 4\int \frac{\mathrm{d}^3k}{(2\pi)^3} n(k), \qquad (38)$$

with ρ the nucleon density.

We have developed computer codes to solve BCS gap equations (eqs. (33)-(38)) following the method introduced by Baldo *et al.* [34]. The approach relies on the introduction of a reduced interaction which disconnects the low and high momentum components of the interaction but reproduces exactly the gap function in the low momentum regime.

In fig. 13 we show results for pairing gaps $\Delta_F = \Delta(k_F)$, in symmetric nuclear matter for $^1S_0$ and $^3SD_1$ states. Empty and filled circles denote the use of BHF potentials in phase I and II, respectively. The inset shows the corresponding chemical potentials at low densities. Gap calculations in the overlapping domain of phases I and II have been performed in a simplified way, namely, pairing in phase I do not take into account phase II and vice versa. This simplification is intended to illustrate the most immediate consequences of the coexisting sp solutions.

Overall we observe that pairing gaps as function of the Fermi momentum, when $k_F \gtrsim 0.3\,\mathrm{fm}^{-1}$, behave similarly to those published elsewhere [1]. The $^1S_0$ state in symmetric nuclear matter yields non-vanishing pairing gap up to $k_F \approx 1.25\,\mathrm{fm}^{-1}$, with a peak $\Delta_F = 2.93\,\mathrm{MeV}$, at $k_F = 0.85\,\mathrm{fm}^{-1}$. Similarly, pairing in the $^3SD_1$ channel occurs up to $k_F \approx 1.8\,\mathrm{fm}^{-1}$, with a peak $\Delta_F = 8.1\,\mathrm{MeV}$, at $k_F = 1.0\,\mathrm{fm}^{-1}$. For $k_F \lesssim 0.3\,\mathrm{fm}^{-1}$, however, the coexisting phases for the sp potentials yield different energy gaps. These features contrast with the continuous low-density solutions for symmetric nuclear matter based on Gogny's interaction [29]. It is also worth noting the correspondence between the Fermi momenta at which BCS pairing disappears and those where dinucleons in normal state within BHF get dissolved (panel (b) of fig. (9)). What also becomes clear is that the maximum pairing gap in the $^1S_0$ channel is about 1/3 that in the $^3SD_1$ state. Considering that *the* gap is given [33] by $\Delta(k)^2 = \Delta_{^1S_0}(k)^2 + \Delta_{^3SD_1}(k)^2 + \cdots$, this results in the actual suppression of $^1S_0$ pairing in symmetric nuclear matter when the coupled $^1S_0$-$^3SD_1$ gap equations are solved. From now on we shall only consider pairing in the $^3SD_1$ channel.

Regarding the low density behavior of the chemical potential shown in the inset of fig. 13, we note that for the deuteron channel $\mu \to -1.1\,\mathrm{MeV}$, close to half the binding energy of the deuteron in free space. This is an expected result as it is well known that gap equations at low densities reduce to the Schrödinger equation in free space, where the anomalous density distribution κ takes the place of the wave function.

In BCS theory the coherence length ξ sets a length scale for the distance between the two constituents forming Cooper pairs. In terms of the anomalous density distribution, this is obtained from

$$\xi^2 = \frac{\int_0^\infty (\frac{\partial \kappa}{\partial k})^2 k^2 \mathrm{d}k}{\int_0^\infty \kappa^2 k^2 \mathrm{d}k}.$$

The evaluation of ξ follows the procedure introduced in the previous section based on Laplace transforms, this time using the anomalous density. In fig. 14 we plot the coherence length as a function of k_F for the $^3SD_1$ channel. The solid curve represents the internucleon separation $\rho^{-1/3}$. Note that the coherence length in phase I amounts between 0.4 and 0.6 times that in phase II. Therefore Cooper pairs in phase I are more compact than those in phase II, in correspondence with dinucleon radii. Additionally, ξ in phase II outpasses the internucleon separation at $k_F \approx 5.5\,\mathrm{fm}^{-1}$, indicating that Cooper pairs extend beyond the mean separation between nucleons. Conversely, at low densities these objects become compact in

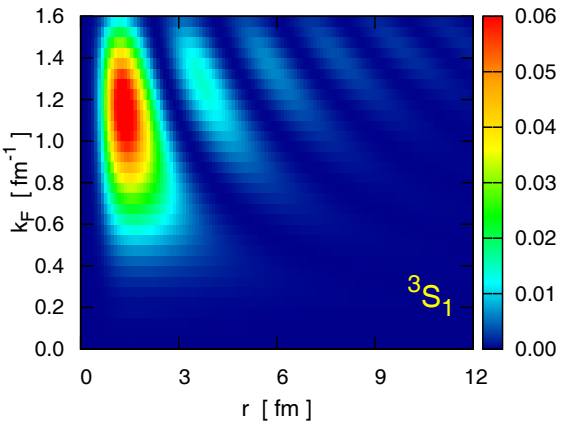

Fig. 15. Contour plot for the $^3S_1$ anomalous probability density $r^2|\Psi(r)|^2$ (in fm^{-1} units) as a function of the relative distance r and Fermi momentum k_F.

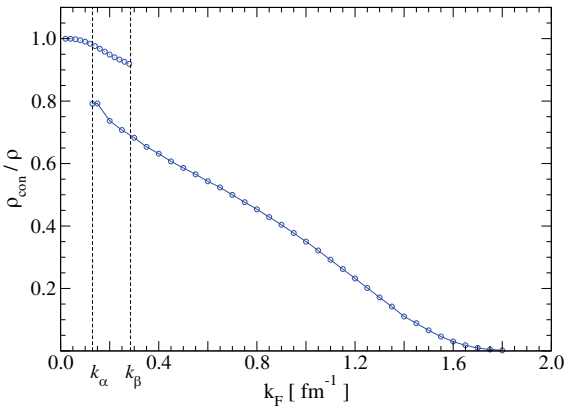

Fig. 16. Condensate fraction in $^3SD_1$ channel as a function of the Fermi momentum, considering sp spectra in phases I and II separately.

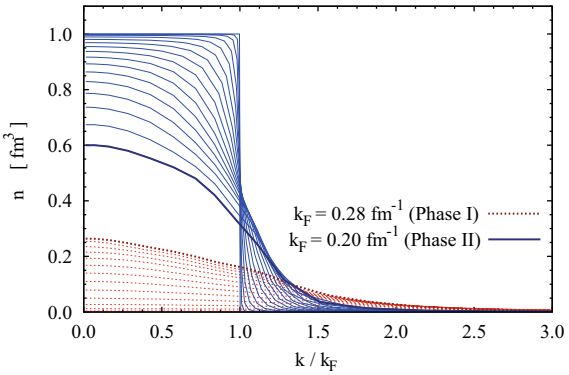

Fig. 17. Normal density as a function of k/k_F for phase I (dashed curves) and phase II (solid curves).

the sense that their size is significantly smaller than the internucleon separation.

In fig. 15 we show a surface plot of the $^3S_1$ anomalous probability density $r^2|\Psi(r)|^2$ calculated from the anomalous density distribution, as a function of the relative distance r and Fermi momentum k_F. These densities have been calculated using the sp potentials in phases I and II. We observe how the distribution spreads over greater extent of space as density increases, consistent with the behavior of the correlation length ξ shown in fig. 14. Additionally, the Fermi momenta at which these functions peak appear in correspondence with the pairing gaps shown in fig. 13.

Having solved gap equations for phases I and II separately, we can now evaluate the condensate fraction in the $^3SD_1$ channel. In terms of the normal and anomalous density distributions the condensate fraction of paired nucleons is given by [35]

$$\frac{\rho_{\rm con}}{\rho} = \frac{\int_0^\infty \kappa^2(k)\, k^2 {\rm d}k}{\int_0^\infty n(k)\, k^2 {\rm d}k}\,. \tag{39}$$

In fig. 16 we plot the deuteron condensate fraction $\rho_{\rm con}/\rho$ as a function of the Fermi momentum. We observe nearly total deuteron condensate (above 90%) at low densities, in phase I, accounting for Bose-Einstein condensation. The condensate fraction in phase II decreases monotonically from 0.8 at $k_F = k_\alpha$, vanishing at $k_F \sim 1.8\,{\rm fm}^{-1}$.

4.4 Superfluidity

As mentioned earlier, the results discussed above help us to visualize the trend of nuclear pairing when each phase is considered separately. Additionally, the sp energies have been obtained within the BHF framework in normal state. The inclusion of superfluidity alters the momentum distribution and subsequently the sp fields [33], leaving open the issue on coexistence of the two phases found for the normal system. A consistent treatment of the problem would require considerably more efforts. Nonetheless, it is possible at the lowest order to estimate some immediate implications of superfluidity on the system along the line discussed in ref. [33].

In fig. 17 we plot the normal density $n(k)$ at various k_F as a function of the ratio k/k_F. Phase-I results (dashed curves) are shown up to $k_F = 0.28\,{\rm fm}^{-1}$, in steps of $0.02\,{\rm fm}^{-1}$. Phase-II results are shown from $k_F = 0.2$ up to $1.8\,{\rm fm}^{-1}$ in steps of $0.1\,{\rm fm}^{-1}$. Note that the momentum distribution at high k_F resembles very closely that of a normal Fermi distribution, consistent with the suppression of BCS pairing. As the density diminishes the momentum distribution spreads over k_F and gets depleted below k_F, in correspondence with the onset of superfluidity. This feature gets more pronounced in phase I.

To gauge the implications in the change of the momentum distribution when pairing is included, we have evaluated the energy per nucleon of the system including the condensation energy [33,36], namely

$$\frac{B}{A} = \frac{1}{\rho}\sum_k \left\{ 4n(k)\left[\frac{k^2}{2m} + \frac{1}{2}U(k)\right] - 2\frac{\Delta^2(k)}{2E(k)}\right\}. \tag{40}$$

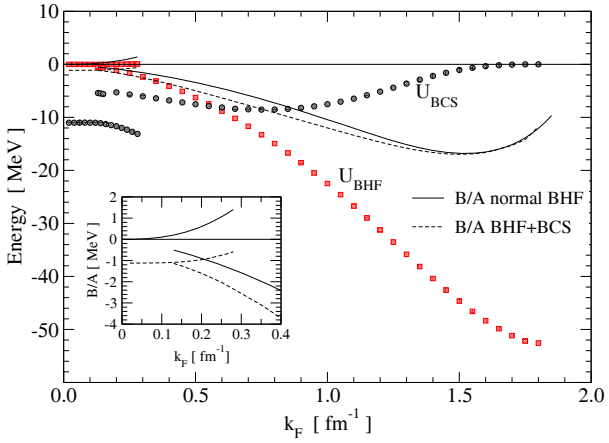

Fig. 18. Calculated B/A as obtained from normal BHF (solid curves) and including condensation energy (dashed curves). The inset shows a close-up at low densities, including solutions in phase I and II. Circles denote the condensation energy (U_{BCS}) and squares the BHF mean-field contribution (U_{BHF}).

The term from this expression which contains the sp fields $U(k)$ is denoted as U_{BHF},

$$U_{BHF} = \frac{2}{\rho}\sum_k n(k)\,U(k)\,, \qquad (41)$$

whereas the last term represents the condensation energy and is denoted by U_{BCS},

$$U_{BCS} = -\frac{1}{\rho}\sum_k \frac{\Delta^2(k)}{E(k)}\,. \qquad (42)$$

For the evaluation of B/A above we use $n(k)$ as obtained from eq. (37) based on sp energies in phase I and II, while the sp potential corresponds to that of normal BHF. Therefore it is not self-consistent in the sense that the evaluation of the sp potentials, $U(k)$, does not take into account the modification of the sp momentum distribution.

In fig. 18 we present the calculated B/A as obtained from normal BHF (solid curves) and that using eq. (40), labeled "BHF+BCS". The inset shows a close-up at low densities, where the solutions from the two phases are displayed. Circles denote the condensation energy (U_{BCS}) and squares the BHF mean field contribution (U_{BHF}). Note that the condensate energy is weak at high densities but increases considerably at low densities, becoming the dominant (attractive) contribution in B/A. The inclusion of pairing in phase I yields $B/A \approx -1.1\,\mathrm{MeV}$, as observed from the inset (dashed curve in phase I). This feature is consistent with the fact that nearly total condensation occurs at low densities. What is also interesting to note is that the condensation energy intercepts U_{BHF} at $k_F \approx 0.55\,\mathrm{fm}^{-1}$, about the same Fermi momentum at which the correlation length ξ outpasses the mean internucleon separation $\rho^{-1/3}$ (see fig. 14). Another result which emerges when pairing correlations are included is a slight decrease of the saturation density, up to about $k_F \approx 1.5\,\mathrm{fm}^{-1}$, without altering the saturation energy.

From the results discussed above it becomes clear that the disentanglement of BHF and superfluidity energies is meaningful at normal densities, *i.e.* near saturation, in contrast to low densities where the condensation energy amounts to a significant contribution to the total energy. This result leaves open the question on whether coexisting solutions persist if a more complete treatment of superfluidity is made.

5 Summary and outlook

Within the BHF approximation in BBG theory for symmetric nuclear matter at zero temperature, we have investigated the role of dinucleon structures over a wide range of densities ($10^{-7}\,\mathrm{fm}^{-3} \lesssim \rho \lesssim 0.36\,\mathrm{fm}^{-3}$), with emphasis placed on the low-density regime. To this end, we have calculated self-consistent sp potentials at Fermi momenta up to $1.75\,\mathrm{fm}^{-1}$ using the continuous choice, restricting the system to normal state. The study is based on the Argonne v_{18} bare NN potential considering all partial waves up to $J = 7\hbar$, without three-body forces. The actual momentum dependence of the sp potential resulting from the evaluation of the mass operator has been retained. An explicit treatment was given to the occurrence of dinucleon bound states in the $^1S_0$ and $^3SD_1$ channels during the evaluation of the mass operator.

As a result, two distinct families of solutions for the sp self-consistent potentials have been disclosed. The first class, U_I, defines a surface in the (k, k_F)-plane at Fermi momenta below $k_\beta = 0.285\,\mathrm{fm}^{-1}$. The second class, U_{II}, defines a surface at Fermi momenta above $k_\alpha = 0.130\,\mathrm{fm}^{-1}$. In the range $[k_\alpha, k_\beta]$ both solutions satisfy the self-consistency requirement, representing coexisting solutions. Solution I behaves as a correlated FG with slight repulsion relative to its non-interacting counterpart. Solution II represents a cohesive system up to the saturation point at $k_F = 1.53\,\mathrm{fm}^{-1}$, where we obtain $B/A = -16.9\,\mathrm{MeV}$ for its binding energy per nucleon. Each solution leads to distinct behaviors in their corresponding effective masses. While the correlated gas phase shows an increasing effective mass, reaching $m^* \approx 3m$ near k_β, the condensed phase starts out with near-bare-mass sp at k_α, reaching a maximum of $1.8m$ at $k_F \approx 0.55\,\mathrm{fm}^{-1}$, and decreasing to about $0.8\,m$ at saturation density. The emergence of massive sp solutions is a peculiarity of our results, in formal resemblance to Heavy Fermions (electrons) observed in unconventional superconductors [37,38]. Work in progress using alternative realistic NN interactions also yields coexisting solutions with large effective masses, confirming the robustness of these findings.

Dinucleon structures associated with phases I and II for the sp fields exhibit unconventional spatial properties, with mean radii as large as $\sim 100\,\mathrm{fm}$. In the case of $^1S_0$ pairs, their size is always greater than the internucleon separation, with a sudden increase in the transit from phase I to phase II. Deuterons wave functions, in turn, appear very confined in phase I but outrange the internucleon separation in phase II.

Findings for nuclear matter in normal state were contrasted with those obtained from BCS pairing states, where BCS gap equations were solved considering sp spectra for phases I and II, independently. Nearly total deuteron condensate is obtained in phase I, decreasing monotonically in phase II up to $k_F = 1.8\,\mathrm{fm}^{-1}$, where ${}^3SD_1$ pairing vanishes. The account for superfluidity lowers, by about 6%, the saturation density of nuclear matter relative to that obtained for normal state. At these densities the condensation energy is much weaker than the sp energy, below 30% for $k_F \gtrsim 1.2\,\mathrm{fm}^{-1}$, justifying the separation between both contributions. Such is no longer the case at low densities where condensation and sp energies become comparable.

The disclosure of coexisting solutions in symmetric nuclear matter at low densities constitutes a major finding in this work. A crucial role was played by the explicit handling of dinucleon bound states together with refined methods to obtain self-consistent solutions for the sp fields. We have shown that the low-density solutions for the sp potentials $U(k)$ are not quadratic in k as they exhibit a sudden change of slope at $k/k_F \approx 1.15$. This feature rules out the reliability of using the effective mass approximation for the sp fields at low densities. In any case, the results reported here demonstrate that self-consistency within the BHF approximation, accounting for dinucleon bound states, is feasible without the need to assume a functional form to the sp fields.

We have next extended the present BHF study to include BCS pairing to lowest order in the sp momentum distribution. From this extension it becomes clear that the separation between BHF and superfluidity energies at low densities is not meaningfull. This leaves open the question as to whether the two coexisting solutions obtained at the BHF level persist if a more complete treatment of superfluidity were made. Actually, we have found that the inclusion of superfluidity attenuates considerably differences in the binding energy of the system in the coexisting range. In this regard, the inclusion of hole-hole propagation needs to be addressed to clarify whether coexisting phases correspond to actual physical properties of nuclear matter at low densities, or they are a result of an oversimplified description. The T-matrix approximation in self-consistent Green's function method [19, 6] offers a more coherent framework to reassess these issues.

The study presented here, where emphasis has been placed on pp correlations with explicit treatment of dinucleon bound states, is basic in the sense that multi-particle and clustering were not taken into account, although they are known to be important in low-density clustering models [26,39,40]. Additionally, three-body forces are known to be crucial to account for the saturation point of nuclear matter [41], so that their effect at normal as well as high densities are expected to be important. However, beyond such simplifying assumptions as embodied by the BHF framework to treat nuclear correlations, it is reasonable to conceive that the model retains leading-order features in diluted nuclear environments expected to linger at low temperatures and isospin asymmetry. In this sense the findings reported in this work may provide additional conceptual tools to better understand the physics of diluted nuclear matter in the context of surface-sensitive nuclear reactions, the coupling to continuum in modeling nuclear open quantum systems [42] or dense star environments. From a more general perspective, it is also reasonable to expect that phase-coexistence in homogeneous nuclear matter in normal state breaks down as temperature and isospin asymmetry reach some critical values. Identifying the conditions under which coexistence persists constitute additional extension of this work.

HFA thanks colleagues at CEA, Bruyères-le-Châtel, France, for their warm hospitality during his stay where part of this work took place. The authors are indebted to M. Baldo and P. Schuck for useful discussions. Funding from CEA/DAM/DIF is acknowledged. This research has been funded in part by FONDECYT under grant No 1120396.

Appendix A. Integral equation with multiple roots on the real axis

A common technique to solve integral equations in momentum space is by discretizing the momentum in the range $q : 0 \to \infty$, reducing the problem to a matrix form. Thus, the equation

$$t(k',k) = v(k',k) + \int_0^\infty \frac{F(k',q)\,\mathrm{d}q}{\omega + i\eta - E(q)} t(q,k)\,,$$

is reduced to the matrix equation

$$t_{ij} = v_{ij} + \sum_{k=1}^{N} \frac{F_{ik}\,w_k}{\omega - E_k}\,t_{kj} - i\pi \sum_{p=N+1}^{N+K} \frac{F_{ip}}{|E'(q_p)|}\,t_{pj}\,. \quad \text{(A.1)}$$

Here we are assuming that there are K solutions to $E(q) = \omega$, with q above the minimum value allowed by Pauli blocking, leading to the set of roots $\{q^{(1)}, \cdots, q^{(K)}\}$. The first sum in eq. (A.1) represents the principal-value integral, for which we apply Gaussian-Legendre quadrature to integrate between consecutive roots, up to infinity.

Appendix B. Adaptive trapezoidal quadrature

Consider the evaluation of the integral

$$I \equiv \int_0^1 f(x)\mathrm{d}x\,, \quad \text{(B.1)}$$

with $f(x)$ any finite function in the range $[0,1]$. This function may also have a finite number of narrow peaks. Let us define

$$I_0 = \frac{1}{2}\left[f(0) + f(1)\right]\,. \quad \text{(B.2)}$$

Additionally, let us consider the following sequence of sets of points in the interval $(0,1)$: $s_1 = \{1/2\}$, $s_2 = \{1/4, 3/4\}$,

$s_3 = \{1/8, 3/8, 5/8, 7/8\}$, etc. Note that the union of the first N sets yields a uniform distribution of points, with no repetition of its elements. If the elements of the union are sequenced in ascending order, the separation between consecutive elements is $1/2^N$. With this construction it can be verified that a trapezoidal quadrature can be represented by the recurrence

$$I_n = \frac{1}{2} I_{n-1} + \frac{1}{2^n} \sum_{x_j \in s_n} f(x_j)\,, \tag{B.3}$$

where I_0 is given by eq. (B.2). In actual evaluations the iteration is interrupted at some $n = M$ when a convergence criteria for $|I_M - I_{M-1}|$ is met. If narrow peaks occur, the minimum n should be such that $1/2^n$ becomes smaller than the smallest width. The advantage of this method is that the historical reckoning of $f(x)$ is not discarded if a narrower mesh is needed. This is an important consideration whenever a single evaluation of f is time-consuming.

Appendix C. Evaluation of Ψ_0 for S and D waves

Let us define

$$\psi_0^{(L)}(q) = A q^L \exp[-R(q-\bar{q})]\Theta(q-\bar{q})\,. \tag{C.1}$$

Denoting $z = \bar{q}R$, and $x = \bar{q}r$, the Fourier transform for $\Psi_0^{(L)}$ for S waves becomes

$$\Psi_0^{(0)}(r) = \sqrt{\frac{2}{\pi}} \frac{A\bar{q}^3}{x(z^2+x^2)^2} \left[(2z+z^2+x^2)x\cos x + (z^2+z^3+zx^2-x^2)\sin x\right]. \tag{C.2}$$

The asymptotic behavior $r \to \infty$ is identified for $x \gg 1$, case in which we get

$$\Psi_0^{(0)}(r) \approx A\bar{q}\sqrt{\frac{2}{\pi}} \frac{\cos(\bar{q}r)}{r^2}\,. \tag{C.3}$$

In the case of D-waves we obtain

$$\begin{aligned}\Psi_0^{(2)}(r) = \sqrt{\frac{2}{\pi}} \frac{-A\bar{q}^5}{x^3(x^2+z^2)^4} \Big\{ \big[x^8 + 3x^6\left(z^2+3z-5\right) \\ + 3x^4 z\left(z^3+7z^2-z-16\right) + x^2 z^4\left(z^2+15z+15\right) \\ + 3z^6(z+1)\big]x\cos(x) + \big[x^8(z-6) - 3z^6(z+1) \\ + x^2z^4(z^3-15z-15) + 3x^6(z^3-4z^2-11z+5) \\ + 3x^4z^2(z^3-2z^2-15z-15)\big]\sin(x)\Big\}\,.\end{aligned} \tag{C.4}$$

This result yields for large distances ($x \gg 1$)

$$\Psi_0^{(2)}(r) \approx -A\bar{q}^3\sqrt{\frac{2}{\pi}} \frac{\cos(\bar{q}r)}{r^2}\,.$$

References

1. R.A. Broglia, V. Zelevinsky (Editors), *Fifty Years of Nuclear BCS* (World Scientific, Singapore, 2013).
2. A. Sedrakian, J.W. Clark, M. Alford (Editors), *Pairing in Fermionic Systems* (World Scientific, Singapore, 2006).
3. Z.H. Li, U. Lombardo, H.J. Schulze, W. Zuo, L.W. Chen, H.R. Ma, Phys. Rev. C **74**, 047304 (2006).
4. P. Gögelein, E.N.E. van Dalen, K. Gad, K.S.A. Hassaneen, H. Müther, Phys. Rev. C **79**, 024308 (2009).
5. W.H. Dickhoff, D. Van Neck, *Many-Body Theory Exposed!* (World Scientific, Singapore, 2008).
6. H. Müther, W. Dickhoff, Phys. Rev. C **72**, 054313 (2005).
7. A. Ramos, A. Polls, W. Dickhoff, Nucl. Phys. A **503**, 1 (1989).
8. M. Baldo (Editors), *Nuclear Methods and the Nuclear Equation of State*, in *International Review of Nuclear Physics*, Vol. **8** (World Scientific, Singapore, 1999).
9. H.Q. Song, M. Baldo, G. Giansiracusa, U. Lombardo, Phys. Rev. Lett. **81**, 1584 (1998).
10. A. Lejeune, C. Mahaux, Nucl. Phys. A **295**, 189 (1978).
11. J. Hüfner, C. Mahaux, Ann. Phys. **73**, 525 (1972).
12. R. Sartor, Phys. Rev. C **27**, 899 (1983).
13. M. Baldo, A. Fiasconaro, Phys. Lett. B **491**, 240 (2000).
14. F.J. Aguayo, H.F. Arellano, Phys. Rev. C **78**, 014608 (2008).
15. H.F. Arellano, J.-P. Delaroche, Phys. Rev. C **83**, 044306 (2011).
16. M.I. Haftel, F. Tabakin, Nucl. Phys. A **158**, 1 (1970).
17. H.F. Arellano, F.A. Brieva, W.G. Love, Phys. Rev. C **50**, 2480 (1994).
18. R.B. Wiringa, V.G.J. Stoks, R. Schiavilla, Phys. Rev. C **51**, 38 (1995).
19. P. Bożek, P. Czerski, Phys. Rev. C **66**, 027301 (2002).
20. M. Baldo, C. Maieron, P. Schuck, X. Viñas, Nucl. Phys. A **736**, 241 (2004).
21. H.V. von Geramb, *The Interaction Between Medium Energy Nucleons in Nuclei* (American Institute of Physics, New York, 1983).
22. K. Amos, P.J. Dortmans, H.V. von Geramb, S. Karataglidis, J. Raynal, in *Advances in Nuclear Physics*, Vol. **25** (Springer, New York, 2000).
23. T.H. Phat, N.T. Anh, D.T. Tam, Phys. Rev. C **84**, 024321 (2011).
24. B. Vonderfecht, C. Gearhart, W. Dickhoff, A. Polls, A. Ramos, Phys. Lett. B **253**, 1 (1991).
25. L.N. Cooper, Phys. Rev. **104**, 1189 (1956).
26. S. Typel, G. Röpke, T. Klähn, D. Blaschke, H.H. Wolter, Phys. Rev. C **81**, 015803 (2010).
27. G. Röpke, Phys. Rev. C **79**, 014002 (2009).
28. M. Baldo, U. Lombardo, P. Schuck, Phys. Rev. C **52**, 975 (1995).
29. M. Matsuo, Phys. Rev. C **73**, 044309 (2006).
30. B.Y. Sun, H. Toki, J. Meng, Phys. Lett. B **683**, 134 (2010).
31. T. Tatsuyuki, R. Tamagaki, Prog. Theor. Phys. Supplement **112**, 27 (1993).
32. D.J. Dean, M. Hjorth-Jensen, Rev. Mod. Phys. **75**, 607 (2003).
33. U. Lombardo, H.J. Schulze, W. Zuo, Phys. Rev. C **59**, 2927 (1999).
34. M. Baldo, J. Cugnon, A. Lejeune, U. Lombardo, Nucl. Phys. A **515**, 409 (1990).

35. L. Salasnich, Phys. Rev. C **84**, 067301 (2011).
36. A.J. Fetter, J.D. Walecka, *Quantum Theory of Many-Particle Systems* (McGraw-Hill Book Company, New York, 1971).
37. G.R. Stewart, Rev. Mod. Phys. **56**, 755 (1984).
38. P. Gegenwart, Q. Si, F. Steglich, Nat. Phys. **4**, 186 (2008).
39. T. Sogo, G. Röpke, P. Schuck, Phys. Rev. C **82**, 034322 (2010).
40. C. Horowitz, A. Schwenk, Nucl. Phys. A **776**, 55 (2006).
41. Z.H. Li, U. Lombardo, H.J. Schulze, W. Zuo, Phys. Rev. C **77**, 034316 (2008).
42. N. Michel, W. Nazarewicz, J. Okolowicz, M. Ploszajczak, J. Phys. G: Nucl. Part. Phys. **37**, 064042 (2010).